3D gradient auxetic soft mechanical metamaterials fabricated by additive manufacturing

Hedayati, Reza; Güven, Aysun; Van Der Zwaag, Sybrand

Important note
To cite this publication, please use the final published version (if applicable).
Please check the document version above.

3D gradient auxetic soft mechanical metamaterials fabricated by additive manufacturing EP

Reza Hedayati, Aysun Güven, and Sybrand van der Zwaag

COLLECTIONS

EP   This paper was selected as an Editor's Pick

View Online   Export Citation   CrossMark

ARTICLES YOU MAY BE INTERESTED IN

Prospects for application of ferroelectric manganites with controlled vortex density
Applied Physics Letters **118**, 140502 (2021); https://doi.org/10.1063/5.0032988

Transverse thermoelectric generation using magnetic materials
Applied Physics Letters **118**, 140504 (2021); https://doi.org/10.1063/5.0046877

Telecom InP-based quantum dash photodetectors grown on Si
Applied Physics Letters **118**, 141101 (2021); https://doi.org/10.1063/5.0045485

3D gradient auxetic soft mechanical metamaterials fabricated by additive manufacturing EP

Reza Hedayati,[a] (iD) Aysun Güven, and Sybrand van der Zwaag (iD)

AFFILIATIONS

Novel Aerospace Materials Group, Department of Aerospace Structures and Materials (ASM), Faculty of Aerospace Engineering, Delft University of Technology (TU Delft), Kluyverweg 1, 2629 HS Delft, the Netherlands

[a]Author to whom correspondence should be addressed: rezahedayati@gmail.com

ABSTRACT

Materials with a negative Poisson's ratio, also known as auxetics, have attracted a lot attention as they have shown innovation potential in applications for energy damping, modern fasteners, biomedical implants, piezoelectric sensors, and soft actuators. In this study, we introduce different patterns of graded distribution of unit cells with positive and negative Poisson's ratio in tubular configurations. Seven types of patterns are programmed into the fabric of the metamaterial to create desired shape changes upon applying far-field external loads. Two of the patterns demonstrate near-zero Poisson's ratio even at axial strains as high as 44%. Other pattern distributions convert the initially cylindrical shape of the tubes to vase, barrel, hourglass, nonsymmetrical vase, and nonsymmetrical hourglass geometries. The experimental Poisson's ratio values for the linear negative-to-positive-to-negative gradient (resulting in hourglass shape) and linear positive-to-negative-to-positive gradient (resulting in barrel shape) cases are $+0.53$ and -0.47, respectively. The measured Poisson's ratio values at tube level are in good accordance with the analytical values of $+0.5$ and -0.5. Benefits of the proposed designs in applications such as action-at-a-distance actuators and wrinkle-free jointless hinges in both 3D and 2D configurations are demonstrated.

Published under license by AIP Publishing. https://doi.org/10.1063/5.0043286

Mechanical metamaterials are materials constructed from repeated unit cells designed to demonstrate mechanical, optical, or acoustical behavior not or rarely found in nature. Such behavior includes negative compressibility,[1] negative mass,[2] meta-fluidity (Pentamode metamaterials),[3,4] and negative Poisson's ratio.[5–7] Poisson's ratio is defined as the (negative) ratio of transverse strain to the longitudinal strain in the case of an applied uniaxial stress. In most natural and man-made materials, the Poisson's ratio has a positive value between 0.2 and 0.5 for most materials, with a few exceptions such as cork,[8] cat's skin,[9] and tendons.[10] Materials with negative Poisson's ratio, also known as auxetics, have attracted a lot attention as they have shown innovation potential in applications for energy damping,[11] fasteners,[12] biomedical implants,[13] piezoelectric sensors,[14] and soft actuators.[5]

Several structural designs have been proposed to create a macroscopically negative Poisson's ratio, including reentrant structures,[15] structures with rotating solid elements,[16] chiral honeycombs,[17] bistable structures,[18] sinusoidal structures,[19] and zigzag structures.[20] Even though some of such brilliant designs can provide very negative values for the Poisson's ratio, they are mechanically weak as they are made up of very fragile building blocks, or alternatively as the solid building blocks are connected together through weak joints. Reentrant structures may provide a good balance of mechanical strength and high levels of negative Poisson's ratio. More importantly, their relatively simple architectures make it possible to vary their geometrical characteristics gradually without major design changes.

Recently, we developed two-dimensional (2D) materials with graded Poisson's ratio as a way of programming localized deformation patterns for application in actuators.[5] A natural pathway forward would be to extend the graded distribution of Poisson's ratio to 3D geometries, as real-life constructions are majorly 3D rather than 2D. In particular, in this study, we focus on the use of gradual distributions in local Poisson's ratio in originally cylindrical shaped specimens. Seven types of patterns were considered to create cylinders with zero Poisson's ratio, vases, hourglasses, barrels, nonsymmetrical hourglasses, and nonsymmetrical barrels from originally cylinders upon the application of an external uniaxial force to the ends of the tubes. The ability to change the shape of an initially cylindrical body to many different shapes can have applications in actuation, clothing, and fastening. Demonstrations of such applications, in particular its use in wrinkleless hinges, are also given.

Tubular specimens with typical cell size dimensions reported in Fig. 1(a) were designed. Figure 1(b) marks the degrees of freedom per unit cell. The tubes reported here were designed on the basis of combinations of reentrant [Fig. 1(c)] and hexagonal cells [Fig. 1(d)]. Seven graded designs were realized: checkered (CH), striped (ST), linear negative to positive (LNP) gradient, linear negative to positive to negative (LNPN) gradient, linear positive to negative to positive (LPNP) gradient, radial negative to positive (RNP) gradient, and radial positive to negative (RPN) gradient, see Fig. 2. In the first two cases (CH and ST), the unit cells with negative and positive Poisson's ratios were organized in arrangements consistent with their labels. The angle in the unit cells with positive and negative Poisson's ratio was, respectively, $\theta = 35°$ and $\theta = -35°$. In the LNP case, the Poisson's ratio of the unit cells varied gradually from negative ($\theta = -40°$) in one side of the cylinder to positive in the other side of the cylinder ($\theta = 40°$). In the LNPN case, the Poisson's ratio of the unit cells was varied from negative in one side ($\theta = -40°$) to positive in the middle of the cylinder ($\theta = 35°$), and then to negative again in the other side ($\theta = -40°$). The opposite arrangement of unit cells was used in LPNP case. In the RNP case, the Poisson's ratio of the unit cells was negative ($\theta = -40°$) at a point in the central ring of the structure, and then it was gradually varied to positive values in both axial and circumferential directions. The opposite was done for the case of RPN ($\theta = 35°$ at the central point).

By the arrangements made, it is expected that in tension, the regions where cells with negative and positive Poisson's ratios are concentrated expand and shrink, respectively. The opposite behavior would occur in compression. In gradient structures, where each row consists of identical unit cells (LNP, LPNP, and LNPN), it is expected that the above-mentioned expansions and shrinkages occur axisymmetrically.

On the other hand, in structures where gradients in unit cells are distributed radially (RNP and RPN), it is expected that expansions/contractions occur locally. Finally, in the structures where unit cells with positive and negative unit cells are arranged in a nondiscriminatory manner (CH and ST), it is expected that the positive and negative unit cells neutralize the effect of each other, and therefore, a non-inflammatory yet non-shrinking behavior is expected (which are also known as structures with zero Poisson's ratio). The above-mentioned regional, axisymmetrical, and non-existing contractions/expansions become very beneficial in several applications, including action-at-a-distance actuation, compliant coatings/clothing, and structures with one-dimensional deformation behavior that will be later on described in more detail.

All the fabricated cylinders had an effective length of $L_c = 181.3$ mm (after deducting the length of the first gripping rows from each side), an inner diameter of $D_i = 43.1$ mm, and an outer diameter of $D_o = 51.1$ mm (hence the average diameter was $D_c = 47.1$ mm). The wall thickness of the cylinder (i.e., the out-of-plane thickness of the cells) was, therefore, $a = 4$ mm. Cylinders with 2.5 mm wall thickness have also been manufactured and tested but found to be too fragile both during sample preparation (removing the support material, see Fig. S2 in the supplementary material) and mechanical testing.

Each cylinder consisted of 30 unit cells in the axial direction and 10 unit cells in the circumferential direction. The first row of cells from each side of the cylinders was used for connecting the specimens to fixtures, which were connected to clamping mechanism of the mechanical test benches. The in-plane thickness of the unit cell walls was $t = 0.8$ mm. For each unit cell, the total height of $H = 6.67$ mm, total width of $W = 14$ mm, and $h = 7.34$ mm were considered (Fig. 1).
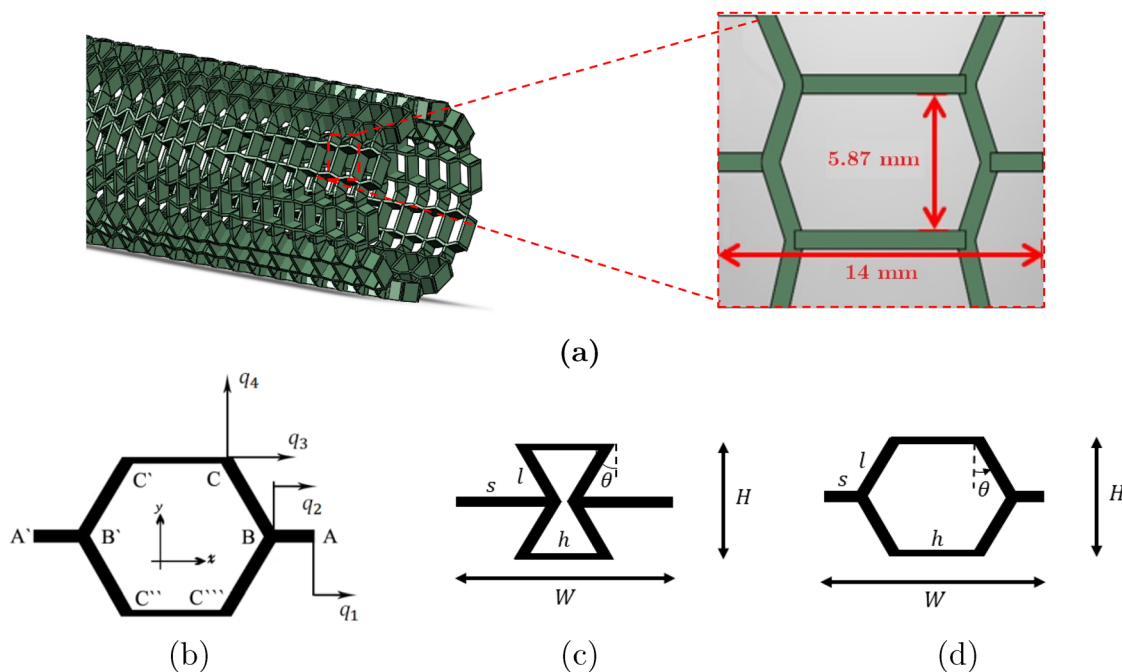

FIG. 1. (a) The geometry and dimensions of unit cells in all the models. (b) Degrees of freedom of the unit cell. (c) and (d) Dimensions of the unit cell in the hexagonal and reentrant unit cells.
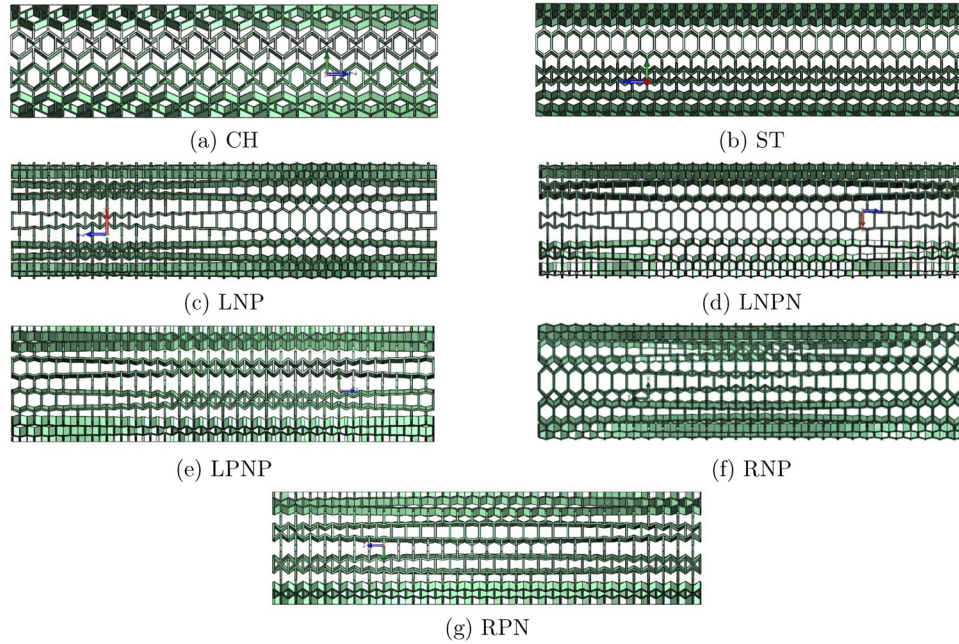
FIG. 2. 3D models of the seven designs: (a) checkered, (b) striped, (c) LNP, (d) LNPN, (e) LPNP, (f) RNP, and (g) RPN.

The specimen designs were generated using SolidWorks API (Application programming interface). The API module assisted in automating redundant and lengthy design tasks in SOLIDWORKS software and creating complex designs introduced in this research. The API module was particularly very beneficial in creating the radial designs (RNP and RPN).

All specimens were manufactured using a mixture of two materials: 60% volume of clear Agilus 30 (Stratasys, MN, USA) as the soft component and 40% of VeroBlackPlus (Stratasys, MN, USA) as the hard component (Table I) resulting in an elastic modulus of 35.88 MPa for the bulk material. The reason for combining soft and hard components was the fact that in specimens made of pure Agilus 30, localized tearing occurred even at small imposed axial strains. Both base materials are photopolymers, which makes them suitable for PolyJet additive manufacturing technology. The specimens were fabricated using Object500 Connex3 3D printer (Stratasys, MN, USA). The specimens were manufactured in the horizontal axial direction to avoid inaccuracies in the manufacturing process due to slight horizontal vibration of the build plate.

All mechanical tests were carried out using a standard mechanical testing machine (ZwickRoell, Germany) with a load cell of 1 kN, and a displacement rate of 4 mm/min was applied. The tensile tests were continued until the first damage in the specimens could be observed (∼80 mm elongation or 44% axial strain). The maximum tensile load applied to all the specimens was about 8 N. The compression tests were continued until global buckling in the cylinders was observed. Unlike the other designs, the checkered design did not show any global buckling, and the compression could be continued until opposing cell walls came into direct physical contact with each other. Poisson's ratios were determined by optically recording the lateral external shape changes and dividing them by the axial elongation applied by the tensile tester.

The stiffness matrix of the unit cells demonstrated in Fig. 1(b) for Euler–Bernoulli beam theory is[21]

$$
\begin{Bmatrix} Q_1 \\ Q_2 \\ Q_3 \\ Q_4 \end{Bmatrix} = \begin{bmatrix} \dfrac{2AE}{s} & -\dfrac{2AE_s}{s} & 0 & 0 \\ -\dfrac{2AE}{s} & \dfrac{4AE_s}{l}\sin^2\theta + \dfrac{48E_sI}{l^3}\cos^2\theta + \dfrac{2AE_s}{s} & -\dfrac{4AE_s}{l}\sin^2\theta - \dfrac{48E_sI}{l^3}\cos^2\theta & \left(\dfrac{4AE_s}{l} - \dfrac{48E_sI}{l^3}\right)\cos\theta\sin\theta \\ 0 & -\dfrac{4AE_s}{l}\sin^2\theta - \dfrac{48E_sI}{l^3}\cos^2\theta & \dfrac{48E_sI}{l^3}\cos^2\theta + \dfrac{4AE_s}{l}\sin^2\theta + \dfrac{4AE_s}{h} & \left(\dfrac{48E_sI}{l^3} - \dfrac{4AE_s}{l}\right)\cos\theta\sin\theta \\ 0 & \left(\dfrac{4AE_s}{l} - \dfrac{48E_sI}{l^3}\right)\sin\theta\cos\theta & \left(\dfrac{48E_sI}{l^3} - \dfrac{4AE_s}{l}\right)\cos\theta\sin\theta & \dfrac{4AE_s}{l}\cos^2\theta + \dfrac{48E_sI}{l^3}\sin^2\theta \end{bmatrix} \begin{Bmatrix} q_1 \\ q_2 \\ q_3 \\ q_4 \end{Bmatrix}, \quad (1)
$$

TABLE I. Material properties of Agilus 30 rubbery and VeroBlackPlus hard materials.

Properties	Agilus 30	VeroBlackPlus
Tensile strength	2.4–3.1 MPa	50–65 MPa
Elongation at break	220–270%	10–25%
Shore hardness	30–35 Scale A	83–86 Scale D
Polymerized density	1.14–1.15 g/cm³	1.17–1.18 g/cm³

where q_i is the displacement at DOF i for $i = 1 - 4$ [Fig. 1(b)] and Q_i is the external force acting on the DOF. E_s is the elastic modulus of the bulk material, A is the area cross section of each unit cell wall, I is the area moment of inertia of each unit cell wall, and s, l, h, and θ are demonstrated in Fig. 1. The corresponding force-displacement relationship for Timoshenko beam theory can be obtained by replacing $\frac{12E_sI}{l^3}$ in the Euler–Bernoulli equation by $\frac{1}{\frac{12E_sI}{l^3} + \frac{l}{2\kappa AG_s}}$,[22] where G_s is the shear modulus of the bulk material and κ is the Timoshenko shear coefficient.

When an external axial force P is acting on the cylinder ends, we have $Q_4 = \frac{2}{10}P$ and $Q_1 = Q_2 = Q_3 = 0$. Inverting the stiffness matrix in Eq. (1) and multiplying them by the force vector, and then using $\nu_{yx} = -\frac{\varepsilon_x}{\varepsilon_y} = \frac{q_1}{q_4}\frac{H}{W}$ gives[21]

$$\nu_{yx} = \frac{H(l^2 - t^2)\sin(2\theta)}{2W\{(l^2 - t^2)\sin^2\theta + t^2\}}, \qquad (2)$$

for Euler–Bernoulli beam theory, and[21]

$$\nu_{yx} = \frac{H(5l^2 + 11\nu_s t^2 + 7t^2)\sin(2\theta)}{W(11\nu_s t^2 + 5l^2 + 17t^2 - (5l^2 + 7t^2 + 11\nu_s t^2)\cos(2\theta))}, \qquad (3)$$

for Timoshenko beam theory.

The above expressions are derived for planar loading conditions. As the diameter of the tube is much larger than the dimensions of the unit cells, the lateral contraction/expansion of the unit cells in the overall tubular configuration can be well approximated by the expression for the case of planar loading, as it will be confirmed in the experimental results to be presented.

For the striped and checkered cases, at each axial plane, the number of cells with positive Poisson's ratio ($\theta_1 = \theta$) equals the number of cells with negative Poisson's ratio ($\theta_2 = -\theta$). Therefore, the total circumferential strain is expected to be zero

$$\varepsilon_c = \frac{H\cos\theta\sin\theta(l^2 - t^2)}{W(t^2\cos^2\theta + l^2\sin^2\theta)} - \frac{H\cos\theta\sin\theta(l^2 - t^2)}{W(t^2\cos^2\theta + l^2\sin^2\theta)} = 0. \quad (4)$$

The analytical Poisson' ratio values will be compared to corresponding experimental values.

The buckling critical load in the inclined walls is $\frac{\pi^2 E_s I}{l^2}$,[21] which means that the buckling load of each unit cell is $P_{cr,UC} = 2\frac{\pi^2 E_s I}{l^2}\cos\theta$, or in other words

$$P_{cr,UC} = \frac{\pi^2 E_s a t^3}{6 l^2}\cos\theta = \frac{2\pi^2 E_s a t^3}{3 H^2}\cos^3\theta. \qquad (5)$$

Therefore, the critical buckling load of the tubes is $P_{cr} = \frac{20\pi^2 E_s a t^3}{3 H^2}\cos^3\theta$. Substituting the dimensional and material values

of the structures gives $P_{cr} = 108.67\cos^3\theta$. For the range of $-40° < \theta < 40°$, we have $48.85\,N < P_{cr} < 108.67\,N$.

All specimens demonstrated the behavior they were designed for. The checkered (CH) and striped (ST) specimens showed negligible circumferential strains under both compressive and tensile loads [as predicted by Eq. (4)]. While the checkered specimen was able to undergo uniform deformation up to 52% under axial compressive strain, the striped specimen buckled at very small compressive displacements (~5% strain). The other specimens also demonstrated early buckling in compressive strain range of 5%–10% due to local bending of the walls. Under tensional loading, the initially perfectly cylindrical shape of LNPN, LPNP, and LNP specimens changed to hourglass, barrel, and vase geometries, respectively (Fig. 3). The shape of RNTP and RPTN specimens also shifted to nonsymmetrical barrel and hourglass shapes, respectively. The maximum circumferential strains in the LNPN (hourglass) and LPNP (barrel) were, respectively, −23% and +21% (Fig. 3). The experimental Poisson's ratio values for the LNPN (hourglass) and LPNP (barrel) cases were, respectively, 0.53 and −0.47 (Table II). The measured Poisson's ratio values were in good agreement with the analytical values [see Eq. (4)], which are 0.5 and −0.5 for LNPN (hourglass) and LPNP (barrel) cases, respectively (6% errors for both cases), see Table II. As for the LNP case (vase), the minimum strain in the shrinking side was −24% and the maximum strain on the inflating side was 3.4%.

The load-displacement curves of almost all geometries were linear in tension. The only exception was the checkered structure, which showed a bi-linear curve with a transition point at an axial strain around 34%. This can be explained as follows. In the majority of specimens, regardless of load value, the horizontal cell walls remain horizontal. However, in the checkered structure, due to the particular arrangement of positive and negative cells, after a certain point, the initially horizontal walls bend upward or downward and take part in load-bearing of the structure. This leads to a sudden increase in the elastic modulus of the structure after a certain strain.

Results presented in Fig. 4 demonstrate that collapse under compressive load occurred at forces ($P_{collapse} < 0.2\,N$) well below the calculated buckling load range ($48.85\,N < P_{cr} < 108.67\,N$). Therefore, the force-displacement curves also confirm that global buckling is triggered by bending in some walls of the lattice structure, rather than local buckling.

In general, the structures demonstrating zero Poisson's ratio (ST and CH) had the lowest moduli (Fig. 4). The elastic moduli of specimens related to barrel, hourglass, and vase shape-shifting had load-displacements curves very close to each other (Fig. 4). The elastic modulus of the RPTN structure was, in general, higher than that of RNTP.

One of the applications of the proposed designs is actuation as encountered in soft robotics. In this method, a final geometry is programed into the fabric of the metamaterial, and the metamaterial can be used as an actuator with specific actuated pattern upon applying external loads on the far-field boundaries of the metamaterial. This type of mechanical actuation provides the user with the advantage of having desired local actuation patterns of different magnitudes without having to deal with other more complex and costly actuation techniques such as hydraulic, pneumatic, heat, and electromagnetic, which, in most cases, would require a large array of expensive local actuators to give non-uniform actuation patterns.
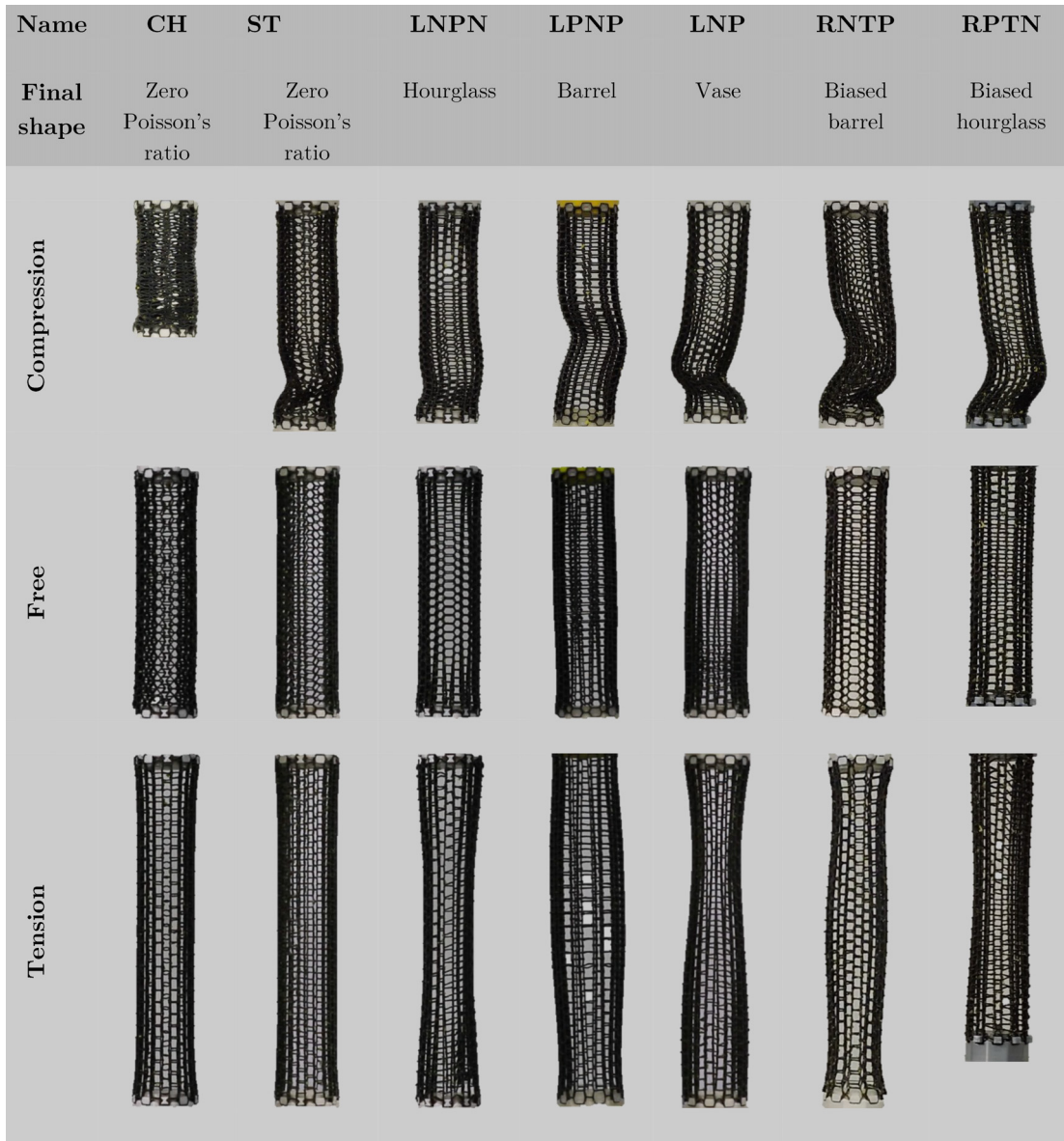
Name	CH	ST	LNPN	LPNP	LNP	RNTP	RPTN
Final shape	Zero Poisson's ratio	Zero Poisson's ratio	Hourglass	Barrel	Vase	Biased barrel	Biased hourglass

FIG. 3. Deformation of the seven designs under tensional and compressive loads.

TABLE II. Comparison of Poisson's ratio values between experimental measurements and the analytical values.

Poisson's ratio	Experimental	Analytical	Error (%)
ST	0	0	0
CH	0	0	0
LNPN	0.53	0.5	6%
LPNP	−0.47	−0.5	6%

Soft robotics and heavy-duty clothing such as space suits, exo-suits, wearable robotics, and diving clothing are the other potential areas of application for the proposed designs. In many body (and equivalent humanoid robots) joints such as arms, fingers, and knees, one needs a pattern which nicely follows the shape of the bending component without local distortions away from the object to be covered. For instance, in a clothing designed to cover the elbow (or similarly a knee), in order to avoid wrinkles, we would need to have shrinkage in the internal part of the elbow and expansion in the external part of elbow when a person closes his arm. A good solution for
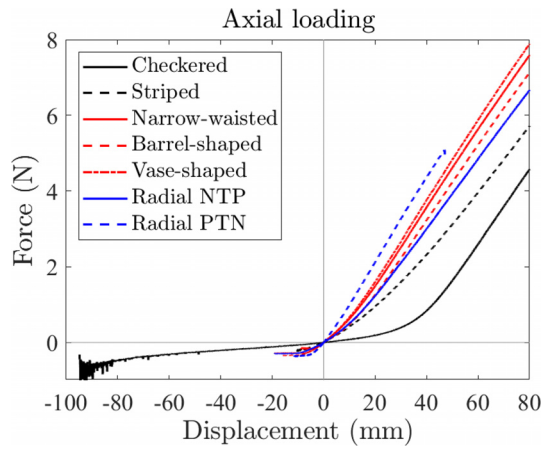
FIG. 4. Force-displacement curves of the seven design under compressive and tensile loads.

that would be the RNP design presented in this paper. To demonstrate this potential, a hinged arm model was covered by the RNP specimen. As it can be seen in Fig. 5(a), when the auxetic part of the design is placed over the internal side of the elbow, no external lateral deformation is observed in the elbow upon bending. However, for the opposite case, a significant level of lateral deformation as well as wrinkles can be observed in the elbow area [Fig. 5(b)]. The reason the RNP design gives wrinkle-free behavior is that in bending (which causes the internal and external sides of the coating to be in compression and tension,
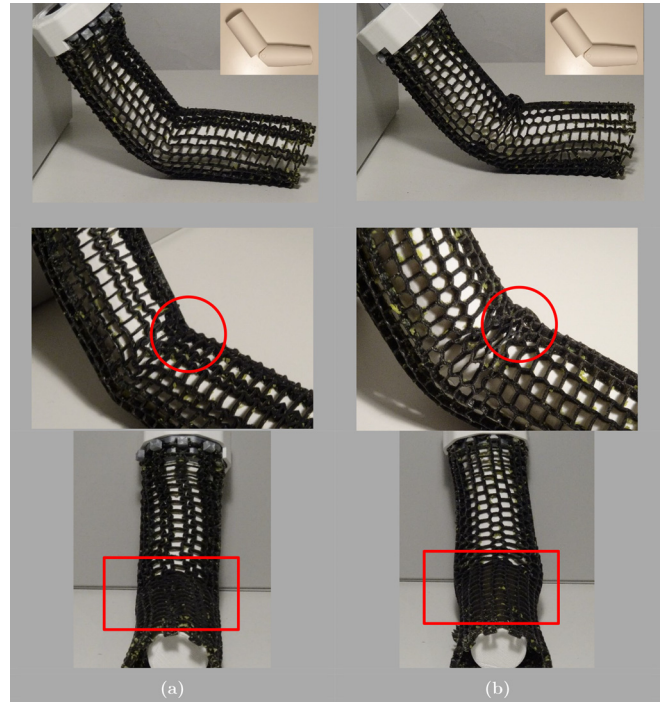

FIG. 5. Arm model covered with RNP design when (a) auxetic part and (b) hexagonal part are covering the internal part of the elbow. In (a), no wrinkles and lateral displacement are observed, while in (b), wrinkles and lateral displacements in the elbow area are visible.
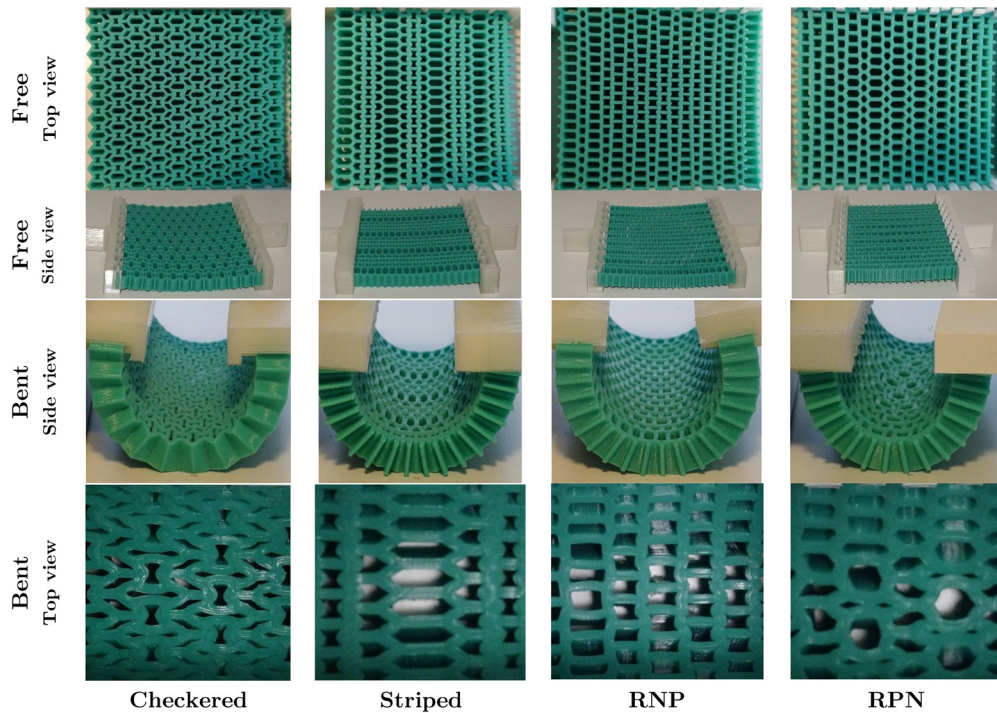

FIG. 6. Comparison of performance of initially flat structures before and after being bent.

respectively), the internal part has negative Poisson's ratio, which means it would shrink, and its external part has positive Poisson's ratio, which leads to expansion in that area. This is the ideal behavior one would expect to avoid wrinkles in a cloth covering a hinge. To enhance the performance of the RNP case even further, one could measure the initial and final circumferential size of a person's arms at different arm locations at both open and closed positions, and then design a structure which accommodates both the initial and final shapes of the arm.

Another important application of 3D gradient auxetic structures is in planar structures exposed to out-of-plane bending. Such initially flat gradient auxetic structures (first presented in Ref. 5) can be used as highly flexible yet durable skins over underlying planar joints. One of the main problems in covering heavy duty joints with a covering skin face is the rupture and failure of skins and its inability to undergo severe flexural rotations repeatedly, as such strains can create significant local and global strains beyond the limit of the material static strength or fatigue endurance. In the present work, several initially flat specimens were manufactured (Fig. 6) using indirect additive manufacturing technique with specifications described in Ref. 5. The specimens had checkered, striped, radial positive to negative (RPN), and radial negative to positive (RNP) patterns. The only difference in the specimens introduced here and the ones presented in Ref. 5 is the in-plane wall thicknesses (0.8 mm in Ref. 5 vs 1.6 mm in the current research). All the specimens were bent over 180°, and their performances were compared. As it can be seen in Fig. 6, the checkered microstructure shows the most promising performance, as it does not show any global lateral deformation, and the local strain at the hinge is contained and distributed uniformly. In the other cases, highly non-uniform local strains were created (for instance, compare the local deformations in the checkered and RPN cases in Fig. 6).

In summary, seven different patterns of hexagonal and reentrant unit cells were programmed into the fabric of tubular specimens with the aim of creating preprogrammed shapes upon applying far-field external loads. Two of the patterns demonstrated zero Poisson's ratio at axial strains as high as 44%. Other pattern distributions converted the initially cylindrical shape of the tube to vase, barrel, hourglass, nonsymmetrical vase, and nonsymmetrical hourglass. Dedicated patterns showed wrinkle-free bending behavior in 3D and 2D applications. Benefits of the proposed designs in applications such as action-at-a-distance actuation and wrinkle-free jointless hinges in both 3D and 2D configurations were presented.

See the supplementary material for photographs of the arm model used in Fig. 5 and a tubular specimen during support material removal procedure.

DATA AVAILABILITY

The data that support the findings of this study are available within the article.

REFERENCES

[1]Z. G. Nicolaou and A. E. Motter, "Mechanical metamaterials with negative compressibility transitions," Nat. Mater. **11**(7), 608–613 (2012).

[2]H. Huang, C. Sun, and G. Huang, "On the negative effective mass density in acoustic metamaterials," Int. J. Eng. Sci. **47**(4), 610–617 (2009).

[3]R. Hedayati, A. Leeflang, and A. Zadpoor, "Additively manufactured metallic pentamode meta-materials," Appl. Phys. Lett. **110**(9), 091905 (2017).

[4]R. Hedayati, S. J. Salami, Y. Li, M. Sadighi, and A. Zadpoor, "Semianalytical geometry-property relationships for some generalized classes of pentamode-like additively manufactured mechanical metamaterials," Phys. Rev. Appl. **11**(3), 034057 (2019).

[5]R. Hedayati, M. Mirzaali, L. Vergani, and A. Zadpoor, "Action-at-a-distance metamaterials: Distributed local actuation through far-field global forces," APL Mater. **6**(3), 036101 (2018).

[6]S. Babaee, J. Shim, J. C. Weaver, E. R. Chen, N. Patel, and K. Bertoldi, "3D soft metamaterials with negative Poisson's ratio," Adv. Mater. **25**(36), 5044–5049 (2013).

[7]F. Javid, J. Liu, J. Shim, J. C. Weaver, A. Shanian, and K. Bertoldi, "Mechanics of instability-induced pattern transformations in elastomeric porous cylinders," J. Mech. Phys. Solids **96**, 1–17 (2016).

[8]L. J. Gibson and M. F. Ashby, *Cellular Solids: Structure and Properties* (Cambridge University Press, 1999).

[9]D. Veronda and R. Westmann, "Mechanical characterization of skin—finite deformations," J. Biomech. **3**(1), 111–124 (1970).

[10]R. Gatt, M. V. Wood, A. Gatt, F. Zarb, C. Formosa, K. M. Azzopardi, A. Casha, T. P. Agius, P. Schembri-Wismayer, and L. Attard, "Negative Poisson's ratios in tendons: An unexpected mechanical response," Acta Biomater. **24**, 201–208 (2015).

[11]Y. Chen, T. Li, F. Scarpa, and L. Wang, "Lattice metamaterials with mechanically tunable Poisson's ratio for vibration control," Phys. Rev. Appl. **7**(2), 024012 (2017).

[12]J. B, Choi and R. S. Lakes, "Design of a fastener based on negative Poisson's ratio foam," Cell. Polym. **10**(3), 205–212 (1991).

[13]O. Abdelaal and S. Darwish, "Analysis, fabrication and a biomedical application of auxetic cellular structures," Int. J. Eng. Innov Technol. **2**(3), 218–223 (2012).

[14]M. L. De Bellis and A. Bacigalupo, "Auxetic behavior and acoustic properties of microstructured piezoelectric strain sensors," Smart Mater. Struct. **26**(8), 085037 (2017).

[15]D. Li, J. Yin, L. Dong, and R. S. Lakes, "Strong re-entrant cellular structures with negative Poisson's ratio," J. Mater. Sci. **53**(5), 3493–3499 (2018).

[16]L. Mizzi, K. M. Azzopardi, D. Attard, J. N. Grima, and R. Gatt, "Auxetic meta-materials exhibiting giant negative Poisson's ratios," Phys. Status Solidi RRL **9**(7), 425–430 (2015).

[17]Y. Sun and N. M. Pugno, "In plane stiffness of multifunctional hierarchical honeycombs with negative Poisson's ratio sub-structures," Compos. Struct. **106**, 681–689 (2013).

[18]K. Bertoldi, P. M. Reis, S. Willshaw, and T. Mullin, "Negative Poisson's ratio behavior induced by an elastic instability," Adv. Mater. **22**(3), 361–366 (2010).

[19]H. Jiang, Z. Zhang, and Y. Chen, "3D printed tubular lattice metamaterials with engineered mechanical performance," Appl. Phys. Lett. **117**(1), 011906 (2020).

[20]J. Liu and Y. Zhang, "Soft network materials with isotropic negative Poisson's ratios over large strains," Soft Matter **14**(5), 693–703 (2018).

[21]R. Hedayati and N. Ghavidelnia, "Analytical relationships for re-entrant honeycombs," EngrXiv (14 December 2020).

[22]R. Hedayati, N. Ghavidelnia, M. Sadighi, and M. Bodaghi, "Improving the accuracy of analytical relationships for mechanical properties of permeable metamaterials," Appl. Sci. **11**(3), 1332 (2021).